Green Chemical Technology

SCIEPublish

Article

Br-Doped Nickel-Cobalt Phosphide Nanoarrays on Engineered Porous NF for High-Efficiency Water Oxidation

Xuanbing Wang [1,2,†], Yang Zhao [1,2,†], Shenhua Yu [1,2], Junli Wang [3], Nan Li [1,2], Linjing Yang [1,2] and Ruidong Xu [1,2,*]

[1] State Key Laboratory of Complex Nonferrous Metal Resources Clean Utilization, Kunming University of Science and Technology, Kunming 650093, China; xuanbingwang@kust.edu.cn (X.W.); zhaoyang1@stu.kust.edu.cn (Y.Z.); yushenghua@stu.kust.edu.cn (S.Y.); 20240259linan@kust.edu.cn (N.L.); eslinjingyang@kust.edu.cn (L.Y.)

[2] Faculty of Metallurgical and Energy Engineering, Kunming University of Science and Technology, Kunming 650093, China

[3] Researcher Center for Analysis and Measurement, Kunming University of Science and Technology, Kunming 650093, China; 20070141@kust.edu.cn (J.W.)

* Corresponding author. E-mail: rdxupaper@kust.edu.cn (R.X.)

† These authors contributed equally to this work.

Received: 31 October 2025; Revised: 18 November 2025; Accepted: 18 March 2026; Available online: 13 April 2026

ABSTRACT: The rational design of cost-effective electrocatalysts for the oxygen evolution reaction (OER) is pivotal for advancing green hydrogen production. This study presents a substrate-engineered Br-doped nickel-cobalt phosphide (NiCoP) electrocatalyst fabricated through a stepwise synthesis protocol. A porous and roughened nickel foam (NF) is initially constructed to provide a 3D conductive scaffold, followed by the hydrothermal growth of vertically aligned NiCo-layered double hydroxide (LDH) nanosheets. Subsequent controlled pyrolysis in the presence of a bromine source yields Br-doped NiCoP nanoarrays securely anchored on the NF/Ni substrate. Comprehensive structural characterization confirms the successful Br incorporation, which induces lattice distortion and optimizes the electronic configuration of NiCoP, while the interconnected porous architecture enhances electrolyte infiltration and gas release. Electrochemical evaluations reveal exceptional OER performance, achieving an ultralow overpotential of 220 mV at 10 mA·cm^{-2} and a Tafel slope of 61.2 mV·dec^{-1} in 1 M KOH, surpassing most reported NiCo-based phosphides. *In-situ* Raman spectroscopy and post-OER characterization uncover dynamic surface reconstruction into Br-enriched (oxy)hydroxide active species, elucidating the dual role of Br as both an electronic modulator and a stabilizer for reactive intermediates. This work demonstrates a substrate-guided heteroatom doping strategy to engineer high-performance bimetallic phosphide electrocatalysts, offering insights into interface engineering for sustainable energy technologies.

Keywords: Oxygen evolution reaction; Br-doped nickel-cobalt phosphide; *In-situ* surface reconstruction; Heteroatom modulation; Electrocatalytic mechanism

© 2026 The authors. This is an open access article under the Creative Commons Attribution 4.0 International License (https://creativecommons.org/licenses/by/4.0/).

1. Introduction

Escalating global energy demand, coupled with the depletion of fossil fuels and severe environmental pollution, has necessitated the urgent development of sustainable and clean energy systems. Hydrogen (H_2), as a carbon-neutral energy carrier with high gravimetric energy density and zero-emission combustion byproducts, has emerged as a promising alternative to traditional fossil fuels [1,2]. Among various hydrogen production technologies, electrochemical water splitting stands out due to its simplicity, scalability, and compatibility with renewable energy sources such as solar and wind. However, the practical implementation of water electrolysis is hindered by the sluggish kinetics of the anodic oxygen evolution reaction (OER), which requires high overpotentials to drive the four-electron transfer process. This inefficiency not only increases energy consumption but also raises operational costs, underscoring the critical need for high-performance OER electrocatalysts to lower reaction barriers and enhance overall system efficiency [3,4].

Significant efforts have been devoted to exploring efficient OER catalysts, primarily focusing on noble metal-based materials (e.g., IrO_2 and RuO_2) due to their superior catalytic activity [5]. Nevertheless, their scarcity, exorbitant cost, and insufficient long-term stability under harsh oxidative conditions have limited their widespread application [6]. Transition metal-based compounds, including phosphides [7,8], sulfides [9,10], and oxides [11–13], have garnered considerable attention as cost-effective alternatives. In particular, nickel-cobalt phosphides (NiCoP) exhibit remarkable OER performance owing to their favorable electronic conductivity and tunable surface properties [14]. Despite these advantages, their catalytic activity and durability remain inferior to noble metal benchmarks, primarily due to limited active sites, poor charge transfer kinetics, and structural degradation during prolonged operation. Recent strategies to address these issues involve nano-structuring [15,16], heteroatom doping [17,18], and heterojunction engineering [19,20]. However, the rational design of electrocatalysts with optimized electronic structures and robust stability remains a formidable challenge, necessitating the continuous exploration of novel modification approaches.

In recent years, halogen doping has emerged as a transformative approach to engineer the electronic, structural, and surface properties of transition metal-based catalysts for the OER, a critical bottleneck in renewable energy technologies such as water splitting and metal-air batteries [21–23]. Unlike conventional heteroatom dopants (e.g., nitrogen or sulfur), halogens (chlorine (Cl), bromine (Br), and iodine (I)) exhibit unique advantages due to their high electronegativity, tunable ionic radii, and strong coordination affinity for transition metal centers. These characteristics enable multifaceted modifications: (i) modulation of d-band electron occupancy to optimize adsorption energies of intermediates; (ii) induction of lattice strain and defects to create abundant active sites; and (iii) stabilization of reconstructed surfaces during electrochemical operation [24–26]. Such synergistic effects collectively enhance both intrinsic activity and reaction kinetics, positioning halogen-doped systems as competitive alternatives to noble-metal-based benchmarks. A paradigmatic example lies in the strategic incorporation of bromide ions (Br^-) into cobalt phosphide (CoP) matrices. Under alkaline conditions, Br^- acts as a dynamic regulator that facilitates the *in-situ* reconstruction of CoP surfaces into an amorphous cobalt (oxy)hydroxide (CoOOH) layer. Crucially, Br^- not only accelerates this dynamic phase transformation but also functions as a "structural stabilizer" by forming strong Co–Br bonds at the interface, thereby mitigating the irreversible degradation of the active layer. Consequently, the optimized Br^--doped CoP catalyst delivers exceptional performance, achieving a low overpotential of 268 mV at 10 $mA \cdot cm^{-2}$, outperforming pristine CoP and many state-of-the-art non-precious-metal catalysts [27]. Similarly, chloride ion (Cl^-) engineering demonstrates distinct merits through defect-mediated reconstruction pathways. When introduced during the synthesis of CoP precursors, Cl^- induces localized lattice distortions and creates coordinatively unsaturated Co sites, which serve as nucleation points for the formation of highly porous, defect-rich CoOOH networks during OER. The resulting hierarchical architecture exposes abundant edge sites and grain boundaries, significantly

accelerating charge transfer and mass transport. As evidenced by electrochemical tests, the Cl^--engineered CoP catalyst achieves an ultralow overpotential of 238 mV at 10 $mA \cdot cm^{-2}$ and maintains remarkable stability over 100 h without significant activity decay [23]. This underscores the critical role of halogen-induced defect engineering in tailoring the morphology and reactivity of reconstructed surfaces.

Despite these promising advances, several fundamental questions remain unresolved, particularly regarding the generalizability of halogen doping across diverse material platforms and operational conditions. For instance, while studies on single-metal systems (e.g., CoP or FeP) have elucidated key mechanisms, the behavior of halogens in bimetallic systems (such as NiCoP) remains poorly understood. Preliminary evidence suggests that halogens may preferentially bind to specific metal sites, altering the relative contributions of Ni and Co to OER activity. However, systematic investigations into the interplay between halogen identity, metal ratio, and dopant location are lacking. Moreover, most prior work focuses on short-term performance metrics, leaving unexplored the long-term structural evolution of halogen-doped catalysts under harsh operating conditions. Addressing these gaps is essential for translating laboratory discoveries into industrially viable applications.

In this study, we report a facile and scalable synthetic approach to fabricate bromine-doped nickel-cobalt phosphide (Br-NiCoP) catalysts via a combined solvothermal and low-temperature phosphidation strategy. The incorporation of Br atoms into the NiCoP lattice effectively regulates the electronic structure of metal active centers, enhances electrical conductivity, and promotes the formation of porous nanostructures with abundant catalytic sites. Systematic electrochemical evaluations demonstrate that the optimized Br-NiCoP catalyst achieves an exceptionally low overpotential of 248 mV at 10 $mA \cdot cm^{-2}$, a small Tafel slope of 38.9 $mV \cdot dec^{-1}$, and outstanding durability over 50 h in alkaline media. Furthermore, the synergistic effects between Ni and Co sites, coupled with the Br-induced surface reconstruction, contribute to the enhanced OER performance. This work not only provides a novel methodology for designing high-efficiency halogen-doped phosphide catalysts but also establishes a comprehensive structure-activity relationship, offering valuable insights into the development of non-precious-metal-based electrocatalysts for sustainable energy conversion technologies.

2. Materials and Methods

2.1. Fabrication of NF/Ni@Br-NiCoP NNs

The NF/Br-NiCoP NNs heterostructure was fabricated through a three-step process involving H_2 bubble-template electrodeposition, hydrothermal treatment, and thermal phosphorization. Initially, a coarsened Ni was deposited onto the surface of NF via electrodeposition in an aqueous solution containing $NiCl_2$ and NH_4Cl at a constant current density of 2 $A \cdot cm^{-2}$. Secondly, vertically aligned NiCo layered double hydroxide (LDH) nanoneedles (NNs) were grown on the nickel foam (NF) substrate via a hydrothermal synthesis protocol. Specifically, an aqueous precursor solution was prepared by dissolving 1 mmol $Co(NO_3)_2 \cdot 6H_2O$, 0.5 mmol $Ni(NO_3)_2 \cdot 6H_2O$, and 4.5 mmol urea in 15 mL deionized water was prepared. The NF support was immersed in this solution and hydrothermally treated at 120 °C for 6 h in a Teflon-lined autoclave. The phosphorization step was performed in a dual-temperature-zone tube furnace. The NF/NiCo LDH NNs precursor (positioned downstream) was thermally converted to NF/Br-NiCoP NNs at 350 °C for 2 h using 0.6 g NaH_2PO_2 as phosphorus source and 0.2 g hexabromobenzene (HBB) as bromine source within the upstream heating zone. Systematic parameter optimization was conducted by preparing comparative samples under varied conditions: phosphorization temperatures (300 °C and 400 °C), NaH_2PO_2 masses (0.4 g and 0.8 g), and HBB quantities (0.1 g and 0.3 g), while maintaining other reaction parameters constant.

2.2. Characterizations

X-ray diffraction (XRD) analyses were performed utilizing Cu Kα radiation (λ = 0.54178 Å) at a scan rate of 5° per minute to ascertain the crystal structure. The valence states of the elements and the chemical composition were evaluated through X-ray photoelectron spectroscopy (XPS, PHI 5500, ULVAC-PHI, Inc., Chigasaki, Japan). The micro- and nanostructural characteristics were elucidated using both transmission electron microscopy (TEM, JEM-2100) and scanning electron microscopy (SEM, Nova SEM 450, FEI Company, Hillsboro, OR, USA), in conjunction with energy dispersive spectroscopy (EDS) for elemental analysis. The electrical conductivity was measured employing the ST2722 semiconductor powder resistivity tester. Additionally, both *ex-situ* and *in-situ* Raman spectroscopic analyses were carried out utilizing a Raman spectroscopy instrument (LabRAM HR, HORIBA Scientific, Piscataway, NJ, USA).

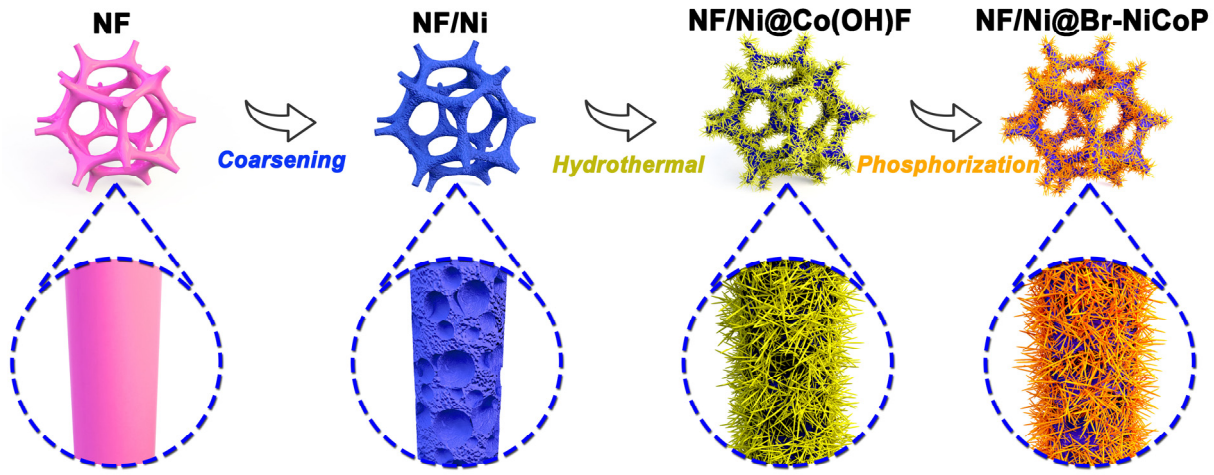
2.3. Electrochemical Measurement

All electrochemical characterizations were conducted using a PARSTAT MC Potentiostat (PMC 2000A, PMC, Princeton Applied Research, Oak Ridge, TN, USA) within a conventional three-electrode configuration. Specifically, a graphite rod was employed as the counter electrode, while a Hg/HgO electrode served as the reference electrode. To minimize the influence of dissolved CO_2 and prevent carbonate formation, all electrolyte solutions were freshly prepared and purged with high-purity N_2 for 30 min prior to the measurements. The working electrode consisted of the as-prepared electrode with a fixed surface area of 0.4 cm^2, and the electrolyte utilized was a 1 M KOH solution. All potentials reported in this study were converted to the reference hydrogen electrode (RHE) using the equation $E_{(RHE)} = E_{(Hg/HgO)} + 0.098 + 0.0591$ pH, and no *iR* correction was applied. Linear scanning voltammetry (LSV) and cyclic voltammetry (CV) measurements were performed at a scan rate of 5 $mV \cdot s^{-1}$. Nyquist plots were generated through electrochemical impedance spectroscopy (EIS) within a frequency range of 0.1 to 10^6 Hz, with an amplitude of 10 mV at a fixed potential of −0.1 V (*vs*. RHE). The resulting data were analyzed and fitted using the EIS spectrum analyzer with an equivalent circuit model represented as R(QR).

3. Results and Discussion

3.1. Synthesis and Structural Characterizations of Catalysts

The NF/Ni@Br-NiCoP was synthesized via a combined hydrothermal and phosphorization process as illustrated in Scheme 1. First, a coarsen NF was prepared via bubble-templated electrodeposition at a high current density of 2 $A \cdot cm^{-2}$ in a solution containing 0.1 M $NiCl_2$ and 2 M NH_4Cl. This specific high current density was employed to induce vigorous hydrogen evolution, where the generated bubbles act as dynamic templates to construct a highly roughened, porous 3D nickel scaffold. While the vigorous hydrogen evolution inevitably leads to local alkalization and the incorporation of trace nickel hydroxides, X-ray diffraction (XRD) analysis confirms that the deposited layer is predominantly metallic Ni (Figure S1). Moreover, the presence of surface hydroxyl species, as identified by XPS (Figure S1b–d), is beneficial as it provides active nucleation sites for the subsequent anchoring and growth of the NiCo LDH precursor in the hydrothermal procedure. Following electrodeposition, a highly roughened surface morphology was obtained (Figure S2). This hierarchical porous architecture is highly beneficial, as it enhances interfacial electrolyte contact and provides efficient mass-transport channels for rapid O_2 bubble detachment [28]. The LSV curves in Figure S3 confirmed the enhanced OER performance. In the subsequent step, a thin layer of NiCo LDH was epitaxially grown onto the NF/Ni framework via a hydrothermal process, wherein the distinct nanoneedle morphology can be visually confirmed (Figure S4). In the last step, the NiCo LDH was converted to Br-doped NiCo phosphide in a tube furnace, with the introduction of $NaHPO_2$ and a certain HBB.



Scheme 1. Synthesis process for NF/Ni@Br-NiCoP.

Systematic characterization was conducted to investigate the phase transformation mechanisms and the microstructural evolution during synthesis. As shown in the XRD patterns (Figure 1a), the hydrothermally prepared NiCo layered double hydroxide (LDH) precursor was completely transformed into hexagonal NiCoP after phosphorization, with distinct diffraction peaks corresponding to the (111), (210), (300), (002), and (400) crystallographic planes. Following the introduction of Br, the peak positions remained largely unchanged, indicating that the incorporation of Br did not alter the phase structure of NiCoP significantly, except for a minor negative shift of approximately 0.2°. This shift can be attributed to the doping effect of Br. According to Bragg's law ($2d\sin\theta = n\lambda$), the successful incorporation of Br—which possesses a comparatively large atomic radius (~1.96 Å), into the NiCoP matrix likely induced a slight volumetric expansion of the unit cell, resulting in the observed negative shift in the diffraction angle (θ).

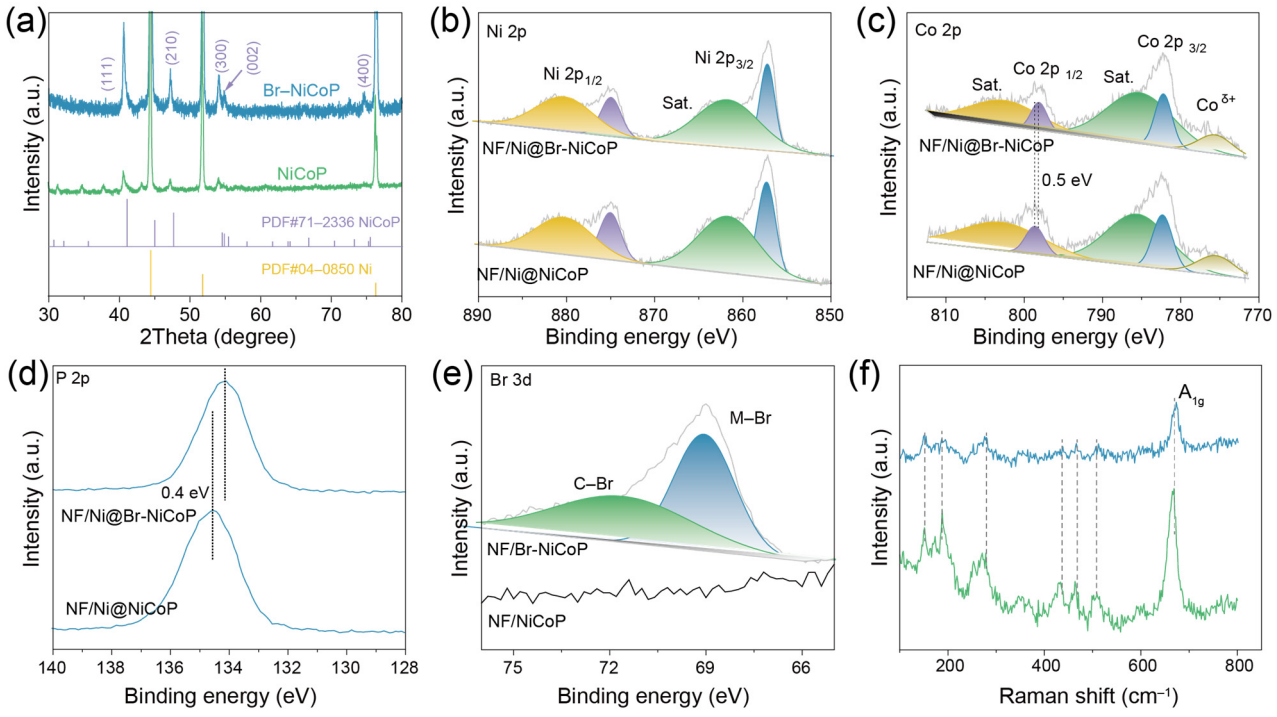


Figure 1. The chemical composition characterization of NiCoP and Br-NiCoP. (**a**) XRD patterns, (**b**) Raman spectra, and high-resolution XPS for (**c**) Ni 2p, (**d**) Co 2p, (**e**) Br 3d, and (**f**) P 2p.

Furthermore, XPS was employed to elucidate the valence states of the elements throughout the synthesis process. The survey spectra (Figure S5) confirm the coexistence of Ni, Co, P, and Br in the Br-NiCoP sample, indicating the successful incorporation of Br. The bulk stoichiometry of Ni, Co, and P was confirmed by ICP-OES (Table S1), while the specific Br content was determined to be approximately 1.13 at.% via semi-quantitative XPS analysis. As shown in Figure 1b, the Ni 2p spectrum can be deconvoluted into two spin–orbit doublets corresponding to Ni^{2+}, located at binding energies of 857.03 eV and 874.92 eV, along with two satellite peaks. Similarly, the Co 2p spectrum (Figure 1c) exhibits three main components and a satellite structure, with peaks at 775.45 eV, 782.13 eV, and 797.82 eV assigned to $Co^{\delta+}$, Co $2p_{3/2}$, and Co^{2+} $2p_{1/2}$, respectively. Upon Br doping, the Co $2p_{1/2}$ peak shifted negatively by 0.5 eV compared to that of pure NiCoP, which can be attributed to the higher electronegativity of Br. In the Br 3d region (Figure 1d), the peaks observed at approximately 68.7 eV and 70.1 eV are assigned to Br $3d_{5/2}$ and Br $3d_{3/2}$, respectively [29]. For the P 2p spectrum (Figure 1e), a peak appears at 134.1 eV, characteristic of PO_4^{3-} species, while the absence of a distinct P 2p signal suggests surface oxidation under ambient conditions. After Br incorporation, the PO_4^{3-} peak exhibited a positive binding energy shift of 0.4 eV relative to that in undoped NiCoP. Combined with the negative shift observed in the Co $2p_{1/2}$ peak, these results suggest that Br doping induces electron redistribution between Co and P, thereby modifying the electronic structure of the electrode. This electronic modulation is conducive to optimizing the adsorption/desorption behavior of reaction intermediates during the OER. The Raman spectra (Figure 1f) for both samples, the peaks at 154 cm^{-1}, 187 cm^{-1}, 271 cm^{-1}, 429 cm^{-1}, 466 cm^{-1} are assigned to the M–P [30], and the apparent peak at 670 cm^{-1} may be corresponded to the A_{1g} model of Ni–O and Co–O, which caused by the inevitably oxidated in air [31–33].

As revealed by SEM images in Figure S4, a uniform thin layer of NiCo layered double hydroxide (LDH) was successfully grown on the NF/Ni substrate via the hydrothermal process. This well-defined nanoarray morphology was well preserved after the subsequent phosphorization treatment, even upon the introduction of HBB, as evidenced in Figure 2a,b. The resulting three-dimensional porous architecture is advantageous, as it promotes the exposure of active sites and facilitates the rapid release of O_2 bubbles during electrocatalysis [34]. Further inspection (Figure 2c) indicates that the individual nanoneedles possess a radius of approximately 10 nm and a length of about 100 nm. To gain deeper insight into the crystalline structure of the as-synthesized Br@NiCoP, TEM and HRTEM were performed (Figure 2d–g). The measured interplanar spacing of 0.22 nm (Figure 2f1,f2) corresponds to the (111) crystal plane of hexagonal NiCoP. Additionally, EDS mapping (Figure 2h) confirms the homogeneous distribution of Ni, Co, P, Br, and O throughout the NF/Ni@Br-NiCoP material, indicating successful and uniform Br doping. Wettability assessments (Figure S6) highlight a remarkable contrast between the samples: NF exhibits hydrophobic behavior, with a water contact angle of 108.99°, whereas NF/Ni@Br-NiCoP displays superhydrophilicity, with a contact angle close to 0°. This pronounced hydrophilic character significantly improves electrolyte permeation and increases the accessible active surface area, thereby benefiting the OER.

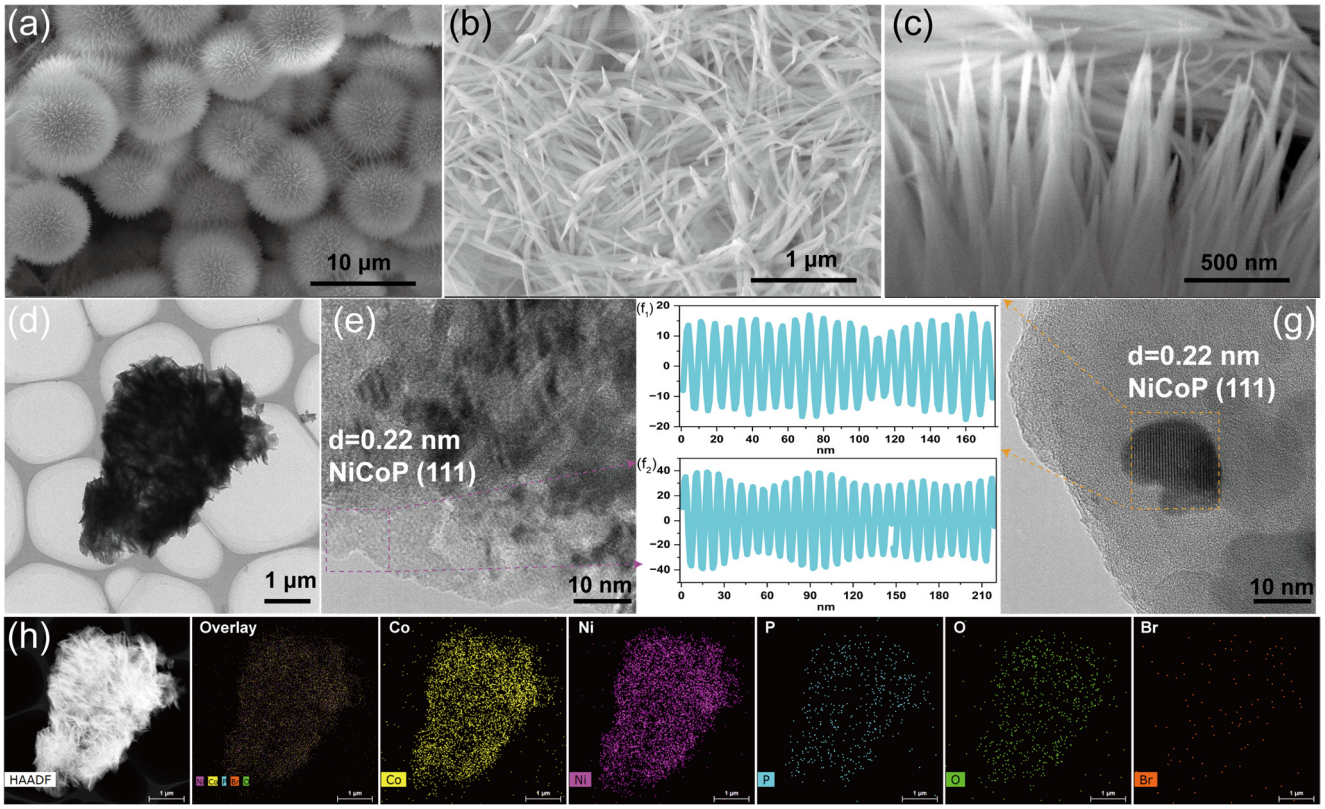


Figure 2. The microstructure characterization of Br-NiCoP. (**a**–**c**) SEM, (**d**) TEM, (**e**,**g**) HRTEM, (**f1**,**f2**) lattice space characterization, and (**h**) EDS mapping.

3.2. Electrocatalytic OER Performance

The OER performance of NF/Ni@Br-NiCoP and the contrast samples was measured by a conventional three-electrode configuration in 1.0 M KOH alkaline electrolyte. As illustrated in Figure 3a,b, The NF/Ni@Br-NiCoP electrocatalyst exhibits the lowest overpotential, requiring only 220 mV to achieve a geometric current density of 10 $mA \cdot cm^{-2}$, while simultaneously delivering an exceptional maximum current density of 387.83 $mA \cdot cm^{-2}$ at 1.6 V *vs*. RHE, surpassing NF/Ni@NiCoP (230 mV, 190.34 $mA \cdot cm^{-2}$), NF/Ni (270 mV, 107.52 $mA \cdot cm^{-2}$), NF (330 mV, 31.44 $mA \cdot cm^{-2}$) and RuO_2 (230 mV, 226.04 $mA \cdot cm^{-2}$). This outstanding electrocatalytic activity eclipses the performance metrics of many recently reported state-of-the-art catalysts, including the Ru/NiFeOOH/NF benchmark [35], $Fe_xNi_{2-x}P_4O_{12}$/RGO [36], Fe_2P/Co_2N porous heterostructure [37], $Co_3(PO_4)_2$ [32], NiFe LDH [38], which are listed in Figure 3g and Table S1. Moreover, it also possesses the largest current densities in the whole studied potential range. Notably, NF/Ni@Br-NiCoP exhibits a remarkably low Tafel slope of 61.2 $mV \cdot dec^{-1}$ in alkaline electrolytes, significantly surpassing commercial RuO_2 (76.0 $mV \cdot dec^{-1}$) and control samples (NF: 115.8 $mV \cdot dec^{-1}$, NF/Ni: 91.9 $mV \cdot dec^{-1}$ and NF/Ni@NiCoP: 81.9 $mV \cdot dec^{-1}$) as evidenced in Figure 3d. This comparison validates the optimized reaction kinetics stemming from enhanced charge transfer efficiency at catalytic interfaces. This minimized Tafel slope indicates that the rate-determining step (RDS) for the OER on this specific surface is the generation of *O intermediates. This kinetic assessment is further corroborated by the methanol oxidation reaction (MOR) probing experiments detailed in Figure S7 [39–41].

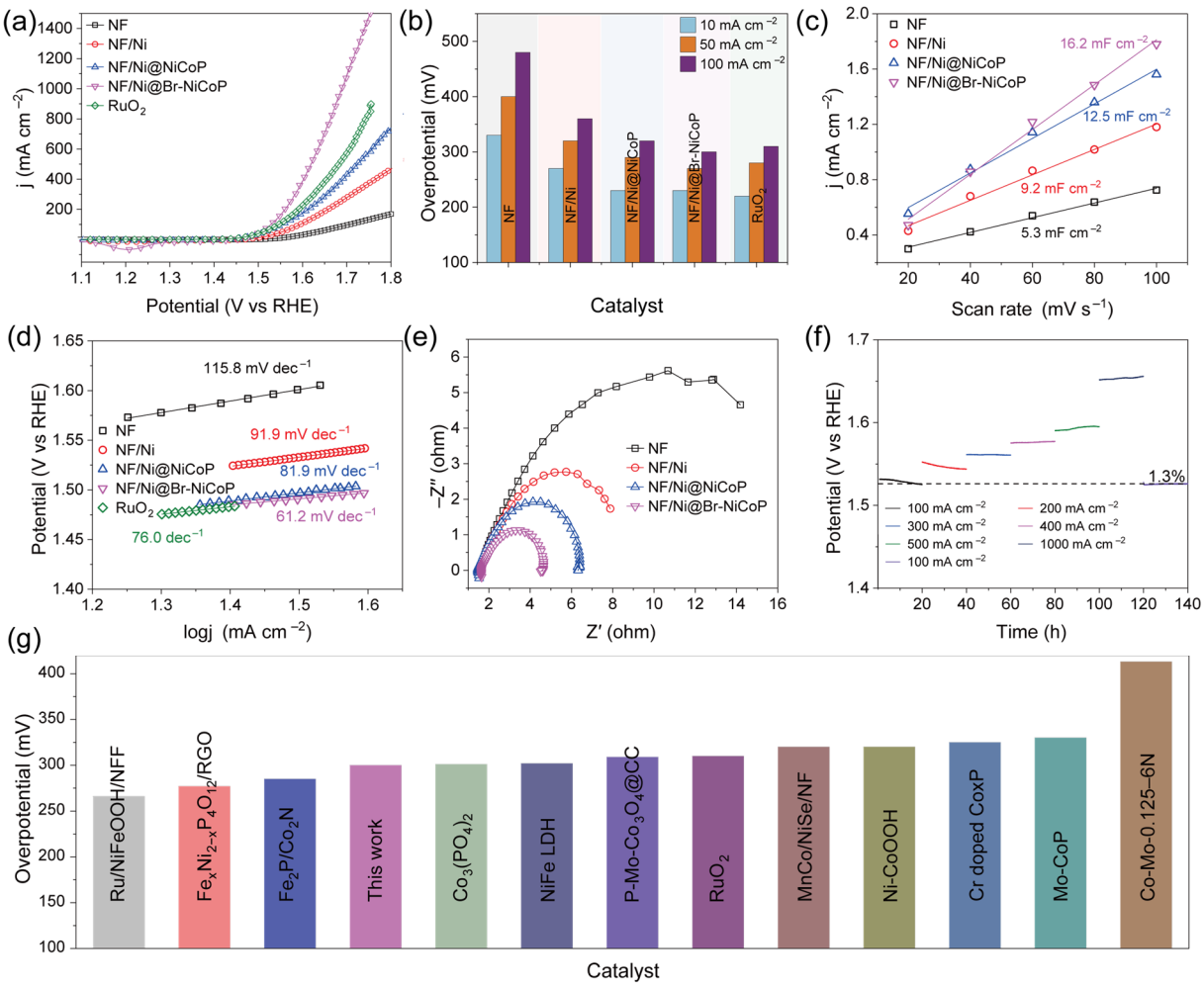


Figure 3. The electrochemical characterization of NF/Ni@Br-NiCoP and the contrast samples. (**a**) LSV curves, (**b**) Overpotentials at 10 mA·cm^{-2} and current densities at 50 mV, (**c**) double layer capacitance fitting plots, (**d**) Tafel fitting lines, (**e**) Nyquist plot, (**f**) constant current polarization curves, and (**g**) Overpotential comparison of NF/Ni@Br-NiCoP at 10 mA·cm^{-2} with recently reported electrocatalysts.

To further contextualize the advancement, systematic benchmarking against state-of-the-art catalysts in Figure 3b elucidates that the developed electrocatalyst retains competitive performance metrics. Apparently, the activity of NF/Ni@Br-NiCoP is comparable with most of the reported catalysts shown in Figures S8 and 3c, NF/Ni@Br-NiCoP exhibits a double-layer capacitance (C_{dl}) of 16.2 mF·cm^{-2}, significantly higher than those of NF/Ni@NiCoP (12.5 mF·cm^{-2}), NF/Ni (9.2 mF·cm^{-2}), and NF (5.3 mF·cm^{-2}), demonstrating its abundant exposed active sites for OER. The ECSA normalized LSV curves in Figure S9 revealed that the NF/Ni@Br-NiCoP NNs remain the best OER activity, indicating the enlarged ECSA is not the only reason behind the enhanced OER activity. It is worth noting that both NF/Ni@NiCoP NNs and NF/Ni@Br-NiCoP NNs have a similar structure and C_{dl} value; however, the NF/Ni@Br-NiCoP NNs show the best OER performance, the reason behind may be the regulated electron structure via Br doping. Electrochemical impedance spectroscopy (EIS) analysis of NF/Ni@Br-NiCoP and reference samples revealed semicircular Nyquist plots with distinct radii (Figure 3e). The R(QR) equivalent circuit model was employed to quantify charge transfer resistance (R_{ct}), demonstrating that NF/Ni@Br-NiCoP achieves the smallest R_{ct} value among all tested materials. This reduced interfacial resistance corresponds to accelerated charge transfer kinetics, consistent with its previously observed minimal Tafel slope. Long-term operational stability is another critical criterion that must be rigorously evaluated for viable electrocatalysts; therefore, continuous constant-current polarization curves were recorded. As depicted in

Figure 3f, the operating potential remained highly stable over a continuous 140-h testing period, unequivocally demonstrating the catalyst's excellent structural durability and robust corrosion resistance during the harsh OER process. Accelerated studies using continuous CV sweeping (6000 cycles at 100 $mV \cdot s^{-1}$) indicated minimal activity degradation, with the final polarization curve overlapping the initial one (Figure S10). Combined with the 140 h CP test, this confirms the exceptional durability of Br-NiCoP under both dynamic and steady-state conditions.

Based on this, the physical characterization was used to investigate the change of NF/Ni@Br-NiCoP after the stability test. The post-test SEM-EDS (Figure S11) elemental mapping visually confirms that Br species remain uniformly distributed across the electrode surface. Consistent with this, the Br signal (Figure S12) can be readily identified in the XPS spectra after the stability test. The persistence of Br indicates that the dopant is structurally stable and resists leaching during the harsh OER process, further corroborating the robust durability of the catalyst. The stability performance of NF/Ni@Br-NiCoP was compared with other transition metal phosphide electrocatalysts reported in recent literature. As summarized in Table S3, while many recently reported analogues typically exhibit stability durations ranging from 24 to 100 h, the as-prepared catalyst demonstrates a superior lifespan of >140 h and robust cycling stability.

3.3. In-Situ Spectroelectrochemistry Analysis

To gain deeper insight into the origin of the enhanced oxygen evolution reaction (OER) performance of NF/Ni@Br-NiCoP, a comparative study was conducted between samples with and without cobalt. As shown in Figure 4a,b, during CV scanning, a distinct oxidation peak associated with cobalt species emerges as the applied potential increases. In contrast, the introduction of nickel results in a broader, more pronounced oxidation signal. This trend is more clearly reflected in the differential pulse voltammetry (DPV) profiles, indicating a more extensive and comprehensive surface oxidation process on the anode. Such multi-step oxidation behavior is advantageous for OER catalysis, as it facilitates the formation of binary active sites involving both Co and Ni species [42], thereby enhancing reaction kinetics through synergistic interactions.

The *in-situ* Raman spectroscopy was systematically performed with a potential increment of 0.05 V. At the open circuit potential (OCP), a vibrational mode at approximately 470 cm^{-1} was observed for both NF/Ni@Br-NiCoP and the pristine NiCoP (Figure 4c,d), which can be attributed to the disordered Ni–O stretching in $Ni(OH)_2$, consistent with previous reports [43]. As the potential increased, two characteristic peaks emerged at 532 cm^{-1} and 550 cm^{-1}, corresponding to NiOOH and Co–NiOOH-type species, respectively. Notably, NF/Ni@Br-NiCoP exhibited a lower onset potential for surface reconstruction by about 50 mV compared to the Br-free sample, indicating facilitated phase transition kinetics induced by Br doping [42]. Furthermore, the CV and DPV profiles of NF/Ni@Br-NiCoP revealed two apparent oxidation peaks at 1.33 V and 1.43 V (*vs*. RHE), assigned to the Ni^{2+}/Ni^{3+} and Co^{3+}/Co^{4+} redox transitions, respectively. In contrast to the NF/Ni@NiCoP reference, the Ni^{2+}/Ni^{3+} oxidation potential was noticeably lowered in the DPV curves. Moreover, additional redox features associated with cobalt species were clearly resolved in NF/Ni@Br-NiCoP, suggesting that Br doping optimizes the electron transfer and redox properties of both Ni and Co sites. This multi-metal redox activity, enhanced by Br incorporation, is likely a key factor contributing to the improved OER performance of the catalyst [44].

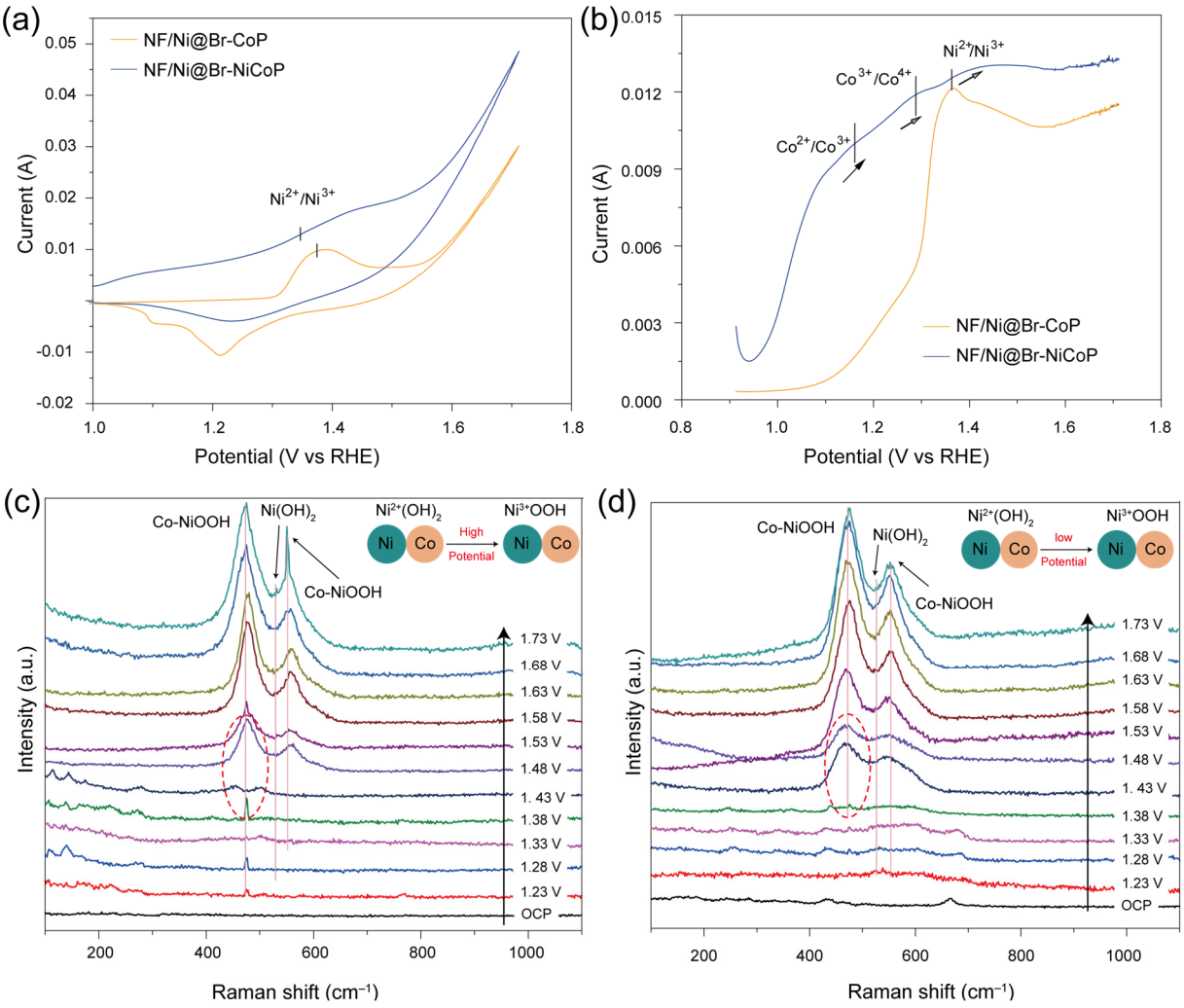


Figure 4. The (**a**) CV and (**b**) DPV curves of NF/Ni@Br-NiP and NF/Ni@Br-NiCoP and *in-situ* Raman spectra for (**c**) NF/Ni@NiCoP and (**d**) NF/Ni@Br-NiCoP.

To confirm the microstructure and chemical composition of the reconstructed surface phase suggested by Raman spectroscopy, *ex-situ* HRTEM and XPS characterizations were conducted post-stability-test electrode. The HRTEM images (Figure S12) reveal well-defined lattice fringes with interplanar spacings of 0.232 nm and 0.149 nm, which correspond to the (002) plane of $Co(OH)_2$ and the (111) plane of $Ni(OH)_2$, respectively. It is notable that while *in-situ* Raman spectroscopy captured the vibrational features of the active oxyhydroxide (NiOOH and CoOOH) species under applied potential, the *ex-situ* HRTEM analysis indicates the presence of hydroxide phases. This apparent discrepancy is attributed to the thermodynamic metastability of high-valence metal oxyhydroxides. As extensively reported in the literature [45,46], active NiOOH/CoOOH species readily undergo reduction to the more stable $Ni(OH)_2$ phase upon removal of the anodic bias and during *ex-situ* sample handling. Thus, the observed hydroxide layer in HRTEM provides strong evidence for surface reconstruction and confirms the precursor phase of the active layer. This transformation is further corroborated by post-OER XPS analysis, which verifies the oxidation of surface metals into high-valence states, along with a significant decrease in P 2p intensity, verifying the sacrificial leaching of phosphorus. Notably, the Br dopant remains stable without significant changes in its chemical state, suggesting its continued role in modulating the electronic structure of the reconstructed active layer during catalysis.

To probe the reaction mechanism, the OER activity was examined as a function of pH. The proton reaction order on the RHE scale ($\rho_{RHE} = \partial_{\log(j)}/\partial_{pH}$) was determined to be approximately 0.99 (Figure 5b).

According to seminal studies by Shao-Horn et al. [42], the pH dependence on the RHE scale serves as a critical descriptor for distinguishing OER pathways. A value of $\rho_{RHE} \approx 0$ typically signifies a concerted proton-electron transfer characteristic of the conventional Adsorbate Evolution Mechanism (AEM). Conversely, a ρ_{RHE} value close to 1, as observed in our NF/Ni@Br-NiCoP catalyst, implies a decoupled proton-electron transfer process. This is a hallmark of the Lattice Oxygen-Mediated (LOM) mechanism, in which the deprotonation of surface lattice oxygen serves as a non-electrochemical rate-determining step [27,47–49]. To strictly validate this kinetic behavior and eliminate potential artifacts arising from ionic strength variations or carbonate interference, the reaction order with respect to hydroxide ions (OH^-) was subsequently determined utilizing tetramethylammonium hydroxide (TMOH) as the supporting electrolyte. Furthermore, the consistent electrochemical performance observed in both KOH and TMOH electrolytes (Figure S14) confirms that the activity is intrinsic and not hindered by carbonate precipitate formation. These combined kinetic analyses strongly suggest that the OER process on NF/Ni@Br-NiCoP is governed by the lattice oxygen pathway, consistent with the observed high activity and pH sensitivity.

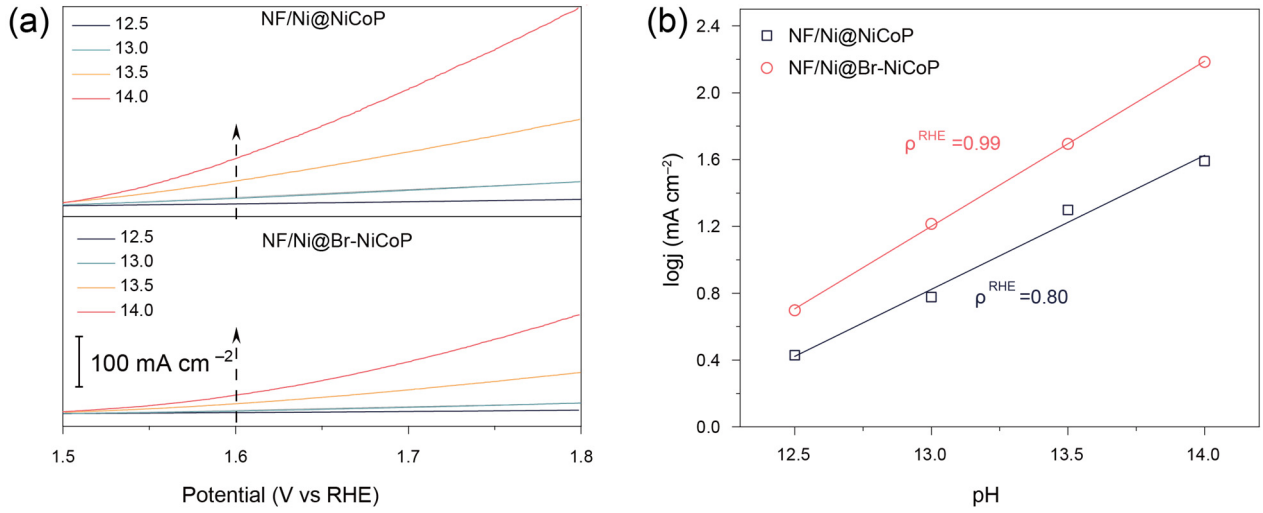


Figure 5. OER performance of the prepared electrodes. (**a**) LSV NF/Ni@Br-NiP and (**b**) NF/Ni@Br-NiCoP under different pH conditions and the $\partial_{\log(j)}/\partial_{pH}$ fitting plots.

4. Conclusions

This study demonstrates a substrate-guided heteroatom-doping strategy to successfully construct bromine-doped nickel-cobalt phosphide (Br–NiCoP) nanoarrays anchored to porous nickel foam. The resulting electrocatalyst exhibits outstanding oxygen evolution reaction (OER) performance in alkaline media, achieving an ultralow overpotential of 220 mV at 10 mA·cm^{-2} and a Tafel slope of 61.2 mV·dec^{-1}, surpassing most reported NiCo-based phosphides. Structural characterization confirms that Br doping induces lattice distortion and optimizes the electronic configuration of NiCoP, while the 3D porous scaffold facilitates electrolyte infiltration and gas release. *In-situ* Raman spectroscopy and post-reaction analysis further reveal a dynamic surface reconstruction into Br-enriched (oxy)hydroxide species as the true active phase during OER. This highlights the dual role of Br as both an electronic modulator and a stabilizer for reactive intermediates. The work provides a viable approach for designing highly efficient and stable bimetallic phosphide electrocatalysts through synergistic substrate engineering and heteroatom doping, offering valuable insights for advancing sustainable energy technologies.

Supplementary Materials

The following supporting information can be found at: https://www.sciepublish.com/article/pii/963, Figure S1: The physical characterization of NF/Ni. (**a**) XRD patterns, XPS of NF/Ni (**b**) survey spectrum

and high resolution XPS of (**c**) Ni 2p and (**d**) O 1s. Figure S2: SEM images of pristine (**a**) NF and NF-Ni deposited for (**b**) 100 s, (**c**) 200 s, (**d**) 300 s, (**e**) 400 s and (**f**) 500 s. Figure S3: Polarization curves for OER of NF and NF-Ni with different deposition time (100 s, 200 s, 300 s, 400 s and 500 s). Figure S4: The SEM images of NF/NiCo LDH in (**a**) low magnification and (**b**) high magnification. Figure S5: The survey XPS spectrum for NF/Ni@Br-NiCoP. Figure S6: The wettability measurements for (**a**) NF and (**b**) NF/Ni@Br-NiCoP. Figure S7: The CV and LSV curves of (**a**,**b**) NF/Ni@NiCoP NNS and (**c**,**d**) NF/Ni@Br-NiCoP. Figure S8: The CV curves in non-faradic region for (**a**) NF, (**b**) NF/Ni, (**c**) NF/Ni@NiCoP and (**d**) NF/Ni@Br-NiCoP. Figure S9: The ECSA normalized LSV curves. Figure S10: The (**a**) CV curves and (**b**) LSV curves for NF/Ni@Br-NiCoP after different CV cycles. Figure S11: The SEM-EDS characterization for NF/Ni@Br-NiCoP post OER test. Figure S12: The XPS characterization for NF/Ni@Br-NiCoP at initial state and post OER test. High resolution XPS spectra for (**a**) Co 2p, (**b**) Ni 2p, (**c**) P 2p and (**d**) Br 3d. Figure S13: The dynamics reconstruction characterization of NF/Ni@Br-NiCoP under OER process. (**a**–**e**) TEM and (HR)TEM and (**f**) EDS spectra. Figure S14: The LSV curves for NF/Ni@NiCoP and NF/Ni@Br-NiCoP in KOH and TMAOH. Table S1: The concentration of Co, Ni P and Br in the NF/Ni@Br-NiCoP. Table S2: The OER overpotential of catalysts reported recently. Table S3: Comparison of OER stability performance of Br-NiCoP with recently reported catalysts.

Acknowledgments

The authors acknowledge the Researcher Center for Analysis and Measurement, Kunming University of Science and Technology, for providing the necessary materials characterization facilities. We are also grateful to Dr. Enze Zhu for their insightful discussions regarding the electrocatalytic mechanism and their helpful suggestions during the manuscript revision process.

Author Contributions

X.W. and Y.Z.: investigation, conceptualization, data curation, formal analysis, writing—original draft, resources, funding acquisition, validation, and supervision. S.Y. and J.W.: investigation, conceptualization, data curation, validation and review & editing. N.L.: data curation and formal analysis. R.X. and L.Y.: conceptualization and data curation.

Ethics Statement

Not applicable.

Informed Consent Statement

Not applicable.

Data Availability Statement

The statement is required for all original articles which informs readers about the accessibility of research data linked to a paper and outlines the terms under which the data can be obtained.

Funding

The authors appreciate the financial support from National Natural Science Foundation of China (No. 52574436), The Industrial Innovation Talent Special Project of Yunnan Province's Xingdian Talent Support Plan (No. yfgrc202417). and the Yunnan Fundamental Research Projects (Grant no. 202301AT070399).

Declaration of Competing Interest

The authors declare that they have no known competing financial interests or personal relationships that could have appeared to influence the work reported in this paper.

References

1. Jiao S, Fu X, Wang S, Zhao Y. Perfecting electrocatalysts via imperfections: Towards the large-scale deployment of water electrolysis technology. *Energy Environ. Sci.* **2021**, *14*, 1722–1770. DOI:10.1039/D0EE03635H
2. Liu R-T, Xu Z-L, Li F-M, Chen F-Y, Yu J-Y, Yan Y, et al. Recent advances in proton exchange membrane water electrolysis. *Chem. Soc. Rev.* **2023**, *52*, 5652–5683. DOI:10.1039/D2CS00681B
3. Tao HB, Liu H, Lao K, Pan Y, Tao Y, Wen L, et al. The gap between academic research on proton exchange membrane water electrolysers and industrial demands. *Nat. Nanotechnol.* **2024**, *19*, 1074–1076. DOI:10.1038/s41565-024-01699-x
4. Sun E, Sarkar A, Gigantino M, Randall R, Jaffer S, Rojas J, et al. Requirements for CO_2-free hydrogen production at scale. *Joule* **2024**, *8*, 1539–1543. DOI:10.1016/j.joule.2024.05.010
5. Shi L, Zhang W, Li J, Yan Q, Chen Z, Zhou X, et al. Recent development of non-iridium-based electrocatalysts for acidic oxygen evolution reaction. *Carbon Neutralization* **2024**, *3*, 1101–1130. DOI:10.1002/cnl2.170
6. Du N, Roy C, Peach R, Turnbull M, Thiele S, Bock C. Anion-Exchange Membrane Water Electrolyzers. *Chem. Rev.* **2022**, *122*, 11830–11895. DOI:10.1021/acs.chemrev.1c00854
7. Zhang Y, Zhang X, Zhang J, Yang C, Li B, Guo J, et al. *In-situ* transcribed local coordinations from CoP nanorods pre-catalyst for efficient electrocatalytic oxygen evolution. *Nano Energy* **2024**, *132*, 110414. DOI:10.1016/j.nanoen.2024.110414
8. Zhang W, Han N, Dou Y, Zhang X, Luo J, Dou S, et al. Applications of Cobalt Phosphide-Based Materials in Electrocatalysis. *ACS Catal.* **2025**, *15*, 5457–5479. DOI:10.1021/acscatal.5c00623
9. Yang H, Chen F, Wang X, Qian J, Wang J, Li J, et al. Self-Reconstructed Spinel with Enhanced SO_4^{2-} Adsorption and Highly Exposed Co^{3+} From Heterostructure Boosts Activity and Stability at High Current Density for Overall Water Splitting. *Adv. Funct. Mater.* **2025**, *35*, 2419978. DOI:10.1002/adfm.202419978
10. Gu P, Song Y, Fan Y, Meng X, Liu J, Wang G, et al. Crystalline-Amorphous Interface-Triggered Electron Redistribution on Copper(II) Sulfide@Metal (Ni, Co, and Fe) Oxyhydroxides for Ultra-Efficient Overall Water/Seawater Splitting. *Adv. Energy Mater.* **2025**, *15*, 2403657. DOI:10.1002/aenm.202403657
11. Zhou A-W, Xu F, Tan J, Liu Z, Zhang G, Xu Z, et al. An Angstrom-Scale Protective Skin Grown *In Situ* on Perovskite Oxide to Enhance Stability in Water. *Angew. Chem. Int. Ed.* **2024**, *64*, e202417360. DOI:10.1002/anie.202417360
12. Zhu Y, Tang Z, Yuan L, Li B, Shao Z, Guo W. Beyond conventional structures: Emerging complex metal oxides for efficient oxygen and hydrogen electrocatalysis. *Chem. Soc. Rev.* **2025**, *54*, 1027–1092. DOI:10.1039/D3CS01020A
13. Ding S, Duan J, Chen S. Recent advances of metal suboxide catalysts for carbon-neutral energy applications. *EcoEnergy* **2024**, *2*, 45–82. DOI:10.1002/ece2.26
14. Ma W, Zhang Y, Wang B, Wang J, Dai Y, Hu L, et al. Significantly enhanced OER and HER performance of NiCo-LDH and NiCoP under industrial water splitting conditions through Ru and Mn bimetallic co-doping strategy. *Chem. Eng. J.* **2024**, *494*, 153212. DOI:10.1016/j.cej.2024.153212
15. Meng N, Feng Y, Zhao Z, Lian F. Boosting the ORR/OER Activity of Cobalt-Based Nano-Catalysts by Co 3d Orbital Regulation. *Small* **2024**, *20*, 2400855. DOI:10.1002/smll.202400855
16. Guo Q, Li R, Zhang Y, Zhang Q, He Y, Li Z, et al. Durable Acidic Oxygen Evolution Via Self-Construction of Iridium Oxide/Iridium-Tantalum Oxide Bi-Layer Nanostructure with Dynamic Replenishment of Active Sites. *Nano Micro Lett.* **2025**, *17*, 165. DOI:10.1007/s40820-025-01680-w
17. Sari FNI, Lai Y-C, Huang Y-J, Wei X-Y, Pourzolfaghar H, Chang Y-H, et al. Electronic Structure Engineering in NiFe Sulfide via A Third Metal Doping as Efficient Bifunctional OER/ORR Electrocatalyst for Rechargeable Zinc-Air Battery. *Adv. Funct. Mater.* **2024**, *34*, 2310181. DOI:10.1002/adfm.202310181
18. Chen Z, Han N, Wei W, Chu D, Ni B-J. Dual doping: An emerging strategy to construct efficient metal catalysts for water electrolysis. *EcoEnergy* **2024**, *2*, 114–140. DOI:10.1002/ece2.29
19. Jia J, Wang Y, Cha Y, Wang Z, Huang J, Wang D, et al. Boosting OER Performance of NiFe-MOFs via Heterostructure Engineering: Promoted Phase Transformation and Self-optimized Dynamic Interface Electron Structure. *Adv. Funct. Mater.* **2025**, *35*, 2500568. DOI:10.1002/adfm.202500568
20. Chen S, Zhang T, Han J, Qi H, Jiao S, Hou C, et al. Interface engineering of Fe-Sn-Co sulfide/oxyhydroxide heterostructural electrocatalyst for synergistic water splitting. *Nano Res. Energy* **2024**, *3*, e9120106. DOI:10.26599/NRE.2023.9120106
21. Ren K, Xu W-J, Li K, Cao J-M, Gu Z-Y, Liu D-H, et al. Br-Induced d-Band Regulation on Superhydrophilic Isostructural

Cobalt Phosphide for Efficient Overall Water Splitting. *Adv. Funct. Mater.* **2025**, *35*, 2415585. DOI:10.1002/adfm.202415585

22. Liu X, Yang S, Huang M, Devasenathipathy R, Huang Q, Huang D, et al. Spatially Confined Electrosynthesis of Halogen-Poor and Carbonyl-Rich Graphene for Boosting Water Desalination and Water Splitting. *Small Methods* **2025**, *9*, 2401591. DOI:10.1002/smtd.202401591
23. Yao J, Zhang Y, Gao F, Jin Q, Zhang L, Xu L, et al. Regulating Reconstruction-Engineered Active Sites of CoP Electrocatalyst by Br Ions During the Oxygen and Hydrogen Evolution Reaction. *Energy Environ. Mater.* **2025**, *8*, e70013. DOI:10.1002/eem2.70013
24. Song H, Yu J, Tang Z, Yang B, Lu S. Halogen-Doped Carbon Dots on Amorphous Cobalt Phosphide as Robust Electrocatalysts for Overall Water Splitting. *Adv. Energy Mater.* **2022**, *12*, 2102573. DOI:10.1002/aenm.202102573
25. Xiao Y, Xia C, Qian Q, Chen J, Wang X, Park HS, et al. Halogen Cocatalysis in Electrocatalytic Systems. *Small* **2025**, *21*, e05412. DOI:10.1002/smll.202505412
26. Cai S, Wang Q, Zhang N, Chen C, Zhang H, Feng Y, et al. Recent Progress in Halogen-Doped Single-Atom Catalysts for Electrochemical Reactions. *Carbon Neutralization* **2025**, *4*, e193. DOI:10.1002/cnl2.193
27. Ye P, Fang K, Wang H, Wang Y, Huang H, Mo C, et al. Lattice oxygen activation and local electric field enhancement by co-doping Fe and F in CoO nanoneedle arrays for industrial electrocatalytic water oxidation. *Nat. Commun.* **2024**, *15*, 1012. DOI:10.1038/s41467-024-45320-0
28. Zhang C, Guo Z, Tian Y, Yu C, Liu K, Jiang L. Engineering electrode wettability to enhance mass transfer in hydrogen evolution reaction. *Nano Res. Energy* **2023**, *2*, e9120063. DOI:10.26599/NRE.2023.9120063
29. Wu Z, Li Q, Xu G, Jin W, Xiao W, Li Z, et al. Microwave Phosphine-Plasma-Assisted Ultrafast Synthesis of Halogen-Doped Ru/RuP2 with Surface Intermediate Adsorption Modulation for Efficient Alkaline Hydrogen Evolution Reaction. *Adv. Mater.* **2024**, *36*, 2311018. DOI:10.1002/adma.202311018
30. Fan H, Jiao D, Fan J, Wang D, Zaman B, Zhang W, et al. Enhancing water-dissociation kinetics and optimizing intermediates adsorption free energy of cobalt phosphide via high-valence Zr incorporating for alkaline water electrolysis. *J. Energy Chem.* **2023**, *83*, 119–127. DOI:10.1016/j.jechem.2023.04.014
31. Zhuo SY, Zhao ZG, Xie ZX, Hao YF, Xu YC, Zhao TY, et al. Complex multiphase organohydrogels with programmable mechanics toward adaptive soft-matter machines. *Sci. Adv.* **2020**, *6*, eaax1464. DOI:10.1126/sciadv.aax1464
32. Begildayeva T, Theerthagiri J, Lee SJ, Yu Y, Choi MY. Unraveling the Synergy of Anion Modulation on Co Electrocatalysts by Pulsed Laser for Water Splitting: Intermediate Capturing by *In Situ*/Operando Raman Studies. *Small* **2022**, 18, 2204309. DOI:10.1002/smll.202204309
33. Wang Y, Kang W, Pu X, Liang Y, Xu B, Lu X, et al. Template-directed synthesis of $Co_2P/MoSe_2$ in a N-doped carbon hollow structure for efficient and stable sodium/potassium ion storage. *Nano Energy* **2022**, *93*, 106897. DOI:10.1016/j.nanoen.2021.106897
34. Zhang J, Zhang Z, Ji Y, Yang J, Fan K, Ma X, et al. Surface engineering induced hierarchical porous $Ni_{12}P_5$-Ni_2P polymorphs catalyst for efficient wide pH hydrogen production. *Appl. Catal. B* **2021**, *282*, 119609. DOI:10.1016/j.apcatb.2020.119609
35. Zhou L, Huang Z-H, Kang F, Lv R. Bimetallic substrate induction synthesis of binder-free electrocatalysts for stable seawater oxidation at industrial current densities. *Chem. Eng. J.* **2023**, *458*, 141457. DOI:10.1016/j.cej.2023.141457
36. Lin L, Wang Y, Ye Q, Zhao Y, Cheng Y. Rapid fabrication of $Fe_xNi_{2-x}P_4O_{12}$ and graphene hybrids as electrocatalyst for highly efficient oxygen evolution reaction. *Appl. Catal. B Environ.* **2023**, *334*, 122834. DOI:10.1016/j.apcatb.2023.122834
37. Zhou X, Mo Y, Yu F, Liao L, Yong X, Zhang F, et al. Engineering active iron sites on nanoporous bimetal phosphide/nitride heterostructure array enabling robust overall water splitting. *Adv. Funct. Mater.* **2023**, *33*, 2209465. DOI:10.1002/adfm.202209465
38. Liu D, Yan Y, Li H, Liu D, Yang Y, Li T, et al. A Template Editing Strategy to Create Interlayer-Confined Active Species for Efficient and Durable Oxygen Evolution Reaction. *Adv. Mater.* **2023**, *35*, 2203420. DOI:10.1002/adma.202203420
39. Tao HB, Xu Y, Huang X, Chen J, Pei L, Zhang J, et al. A General Method to Probe Oxygen Evolution Intermediates at Operating Conditions. *Joule* **2019**, *3*, 1498–1509. DOI:10.1016/j.joule.2019.03.012
40. Chen H, Chen J, Ning P, Chen X, Liang J, Yao X, et al. 2D Heterostructure of Amorphous CoFeB Coating Black Phosphorus Nanosheets with Optimal Oxygen Intermediate Absorption for Improved Electrocatalytic Water Oxidation. *ACS Nano* **2021**, *15*, 12418–12428. DOI:10.1021/acsnano.1c04715
41. Mei Y, Feng Y, Zhang C, Zhang Y, Qi Q, Hu J. High-Entropy Alloy with Mo-Coordination as Efficient Electrocatalyst for Oxygen Evolution Reaction. *ACS Catal.* **2022**, *12*, 10808–10817. DOI:10.1021/acscatal.2c02604
42. Grimaud A, Diaz-Morales O, Han B, Hong WT, Lee Y-L, Giordano L, et al. Addendum: Activating lattice oxygen redox reactions in metal oxides to catalyse oxygen evolution. *Nat. Chem.* **2017**, *9*, 828. DOI:10.1038/nchem.2819

43. Shi G, Li J, Lu T, Yang C, Xu Q, Gu H, et al. Lattice O–O ligands in Fe-incorporated hydroxides enhance water oxidation electrocatalysis. *Nat. Chem.* **2025**, *17*, 1607–1614. DOI:10.1038/s41557-025-01898-6
44. Wang X, Pi W, Hu S, Bao H, Yao N, Luo W. Boosting Oxygen Evolution Reaction Performance on NiFe-Based Catalysts Through d-Orbital Hybridization. *Nano-Micro Lett.* **2024**, *17*, 11. DOI:10.1007/s40820-024-01528-9
45. Trotochaud L, Young SL, Ranney JK, Boettcher SW. Nickel–Iron Oxyhydroxide Oxygen-Evolution Electrocatalysts: The Role of Intentional and Incidental Iron Incorporation. *J. Am. Chem. Soc.* **2014**, *136*, 6744–6753. DOI:10.1021/ja502379c
46. Grimaud A, Diaz-Morales O, Han B, Hong WT, Lee Y-L, Giordano L, et al. Activating lattice oxygen redox reactions in metal oxides to catalyse oxygen evolution. *Nat. Chem.* **2017**, *9*, 457–465. DOI:10.1038/nchem.2695
47. Huang Q, Xia G-J, Huang B, Xie D, Wang J, Wen D, et al. Activating lattice oxygen by a defect-engineered Fe_2O_3–CeO_2 nano-heterojunction for efficient electrochemical water oxidation. *Energy Environ. Sci.* **2024**, *17*, 5260–5272. DOI:10.1039/D4EE01588F
48. He Z, Zhang J, Gong Z, Lei H, Zhou D, Zhang N, et al. Activating lattice oxygen in NiFe-based (oxy)hydroxide for water electrolysis. *Nat. Commun.* **2022**, *13*, 2191. DOI:10.1038/s41467-022-29875-4
49. Wang F, Xu X, Li Y, Gu L, Li L, Liu H, et al. Triggering lattice oxygen in *in-situ* evolved CoOOH for industrial-scale water oxidation. *Appl. Catal. B Environ. Energy* **2025**, *363*, 124838. DOI:10.1016/j.apcatb.2024.124838